JOURNAL OF GEOPHYSICAL RESEARCH, VOL. 111, B12402, doi:10.1029/2005JB004014, 2006

Current slip rates on conjugate strike-slip faults in central Tibet using synthetic aperture radar interferometry

Michael Taylor[1,2] and Gilles Peltzer[1,3]

Received 28 August 2005; revised 18 July 2006; accepted 15 August 2006; published 9 December 2006.

[1] We estimate the current slip rates on active conjugate strike-slip faults in central Tibet using repeat-pass synthetic aperture radar interferometry (InSAR). The conjugate fault systems are centered along the east trending Late Jurassic–Early Cretaceous Bangong-Nujiang suture zone and are composed of NE striking left-slip faults to the north and NW striking right-slip faults to the south. The surface displacement field obtained from InSAR data show 30- to 60-km-wide zones of concentrated shear that coincide with active fault traces observed in the field. The radar data indicate that, within a 200- to 300-km-wide belt, the deformation regime defined by the conjugate strike-slip faults is accommodating $\sim$5 mm yr^{-1} of pure shear contraction oriented in the N10°E direction and $\sim$6 mm yr^{-1} of right-lateral simple shear in the N110°E direction. The observation of localized strain along faults indicates that faulting is the dominant mode of deformation in central Tibet with seismogenic depths extending down to $\sim$25 km. Furthermore, extrapolating the current slip rates estimated for the central Tibet faults, the total magnitude of fault slip based on geological observations would only require the faults to have initiated sometime in the past 2–3 Myr. This appears to contradict the few geochronologic constraints on fault initiation at 8 Ma or even earlier. This discrepancy suggests that the fault slip rates may not have remained constant through time but have accelerated in the recent period. With the exception of the slip rate on the Gyaring Co fault, the slip rates that we determined on the conjugate strike-slip faults in central Tibet are significantly slower than the rates on faults that bound the Tibetan Plateau, such as the left-slip Altyn Tagh fault to the north. This observation suggests that although deformation is active within central Tibet, plateau-bounding structures are dominant in absorbing Indo-Asian convergence.

Citation: Taylor, M., and G. Peltzer (2006), Current slip rates on conjugate strike-slip faults in central Tibet using synthetic aperture radar interferometry, *J. Geophys. Res.*, *111*, B12402, doi:10.1029/2005JB004014.

1. Introduction

[2] While lithospheric thickening prior to and since the Indo-Asian collision has created the Tibetan Plateau [*Burg et al.*, 1984; *Murphy et al.*, 1997; *Tapponnier et al.*, 2001; *Yin and Harrison*, 2000], mixed-mode faulting composed of normal and strike-slip fault systems dominate the current map pattern of active structures within its interior. Understanding the present-day kinematics of the Indo-Asian collision requires identifying individual faults and quantifying their rates of motion. We estimate for the first time, the current fault slip rates on a set of conjugate strike-slip faults in central Tibet [*Taylor et al.*, 2003] extending roughly from Shiquanhe in western Tibet to Jiali in eastern Tibet, which are prominent in the physiography of the Tibetan Plateau. *Armijo et al.* [1989] recognized the southern, right-lateral portion of this en echelon fault system as the Karakoram-Jiali fault zone (KJFZ) (Figure 1) and proposed it to be the structure along which eastward movement of the Qiangtang terrane relative to the Lhasa terrane is localized (Figure 1). Thus the KJFZ was interpreted to have major geologic and geodynamic significance with respect to the deformation of continental crust in Asia, acting as a conjugate fault to the lithospheric-scale Kunlun and Altyn Tagh strike-slip faults (ATF) in the north [*Armijo et al.*, 1989]. However, *Taylor et al.* [2003] recently observed that the right-lateral faults in the KJFZ are paired with left-lateral faults to the north and suggested that these faults form a series of conjugate strike slip systems that allow distributed east west extension and coeval north south contraction of central Tibet.

[3] Constraints on the geodetic rate and distribution of active faulting within central Tibet have been incomplete due to the reconnaissance nature of geologic studies and Global Positioning System (GPS) surveys in the region.

[1]Department of Earth and Space Sciences, University of California and Institute of Geophysics and Planetary Physics, Los Angeles, California, USA.
[2]Now at Department of Geology, University of Kansas, Lawrence, Kansas, USA.
[3]Also at Jet Propulsion Laboratory, California Institute of Technology, Pasadena, California, USA.

0148-0227/06/2005JB004014$09.00

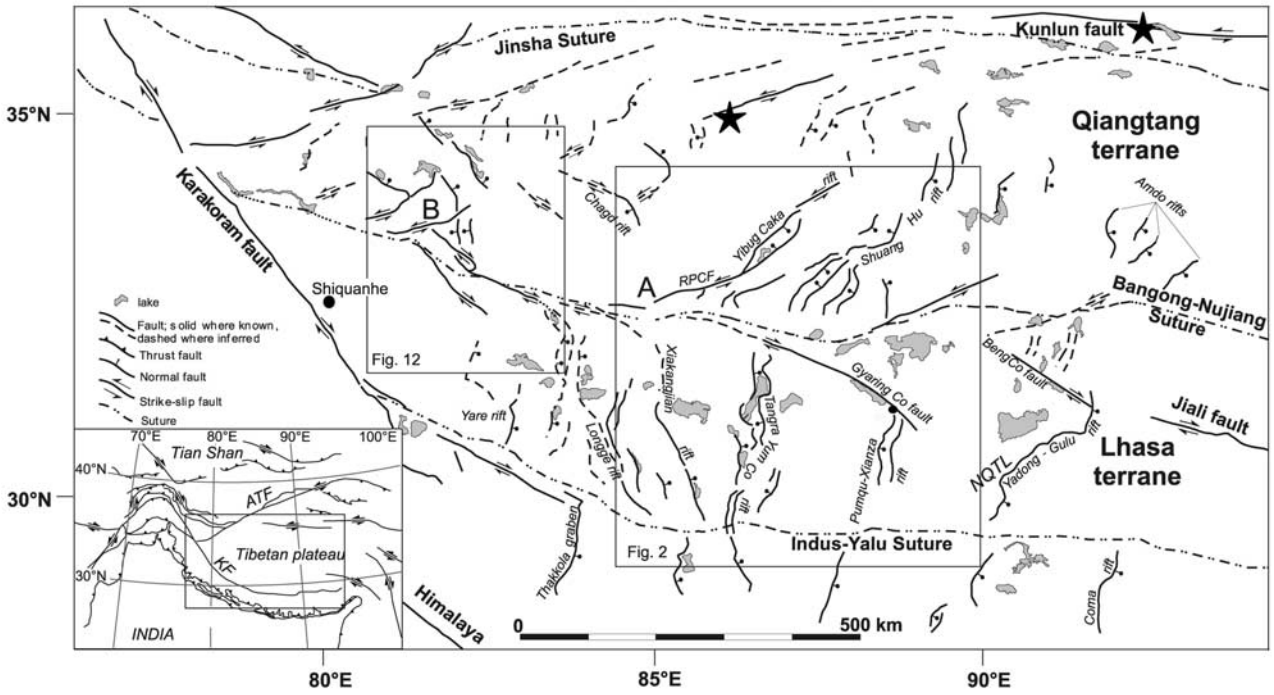

Figure 1. Map of active faults in central and southern Tibet based on previous investigations of *Taylor et al.* [2003] and *Armijo et al.* [1986, 1989] and new observations from satellite images. Boxes indicate areas covered by Figures 2 and 12. RPCF, Riganpei Co fault; A, Dong Co conjugate fault system; B, Bue Co conjugate fault system; NQTL, Nyainqentanglha Shan. Stars indicate epicenters of the 1997 M 7.6 Manyi (west) and 2001 M 7.9 Kokoxilli (east) earthquakes. Inset shows map of Indo-Asian collision for location.

Wang et al. [2001] used a sparse north south transect of campaign style GPS surveys along the Golmud-Lhasa highway near longitude 95°E to quantify the deformation field from the Himalaya to the Qiadam basin across south and central Tibet. Their GPS velocity field suggested ~5 mm yr^{-1} of shortening parallel to the N20°E direction and ~7 mm yr^{-1} of right-lateral shear in the N110°E direction between the Tanghla Nan Shan area in the north and the city of Lhasa to the south [*Wang et al.*, 2001]. A recent compilation of the GPS velocity data collected by several groups during 1998 and 2002 indicates a similar velocity field [*Zhang et al.*, 2004]. However, due to the sparseness of the geodetic arrays, the particular faults accommodating the deformation in central Tibet were not identified in those studies.

[4] In this paper, we investigate active surface deformation in the southern Qiangtang and northern Lhasa terranes along faults in the KJFZ [*Armijo et al.*, 1989; *Molnar and Tapponnier*, 1978; *Tapponnier and Molnar*, 1977] and associated conjugate faults to the north [*Taylor et al.*, 2003]. We use the technique of synthetic aperture radar interferometry (InSAR) to estimate the current interseismic surface movement along these prominent faults. Our investigation focuses on two regions of the central Tibetan Plateau where previous bedrock and neotectonic mapping has revealed the geometry and kinematics of conjugate strike-slip fault systems (Figure 1) [*Armijo et al.*, 1989; *Taylor et al.*, 2003]. The first structure is the Dong Co conjugate strike-slip fault system, which is centered on the Bangong-Nujaing suture zone and is composed of the left-slip Riganpei Co fault to the north and the right-slip Gyaring Co fault to the south (Figure 1). The second conjugate strike-slip fault system is located ~400 km to the west and is referred to as the Bue Co conjugate fault system (Figure 1). The Bue Co left-slip fault defines the northern fault segment and the Lamu Co right-slip fault defines the southern fault segment (Figure 1). These conjugate fault systems bound a series of crustal wedges distributed throughout central Tibet [*Armijo et al.*, 1989; *Taylor et al.*, 2003; *Yin et al.*, 1999].

[5] In the following sections, we first describe the approach used in the radar data analysis and model parameter fit. We then present the structural framework for each conjugate strike-slip fault system and place the radar observations into a geologic context. Finally, we discuss the implications of our estimated current fault slip rates in a regional tectonic framework, which impacts our understanding of the mechanics of the Indo-Asian collision.

2. Data Analysis

2.1. Radar Data Selection and Processing

[6] The European Space Agency (ESA) satellites ERS1 and ERS2 have been acquiring C-band synthetic aperture radar (SAR) data since 1991. Over Tibet, the archive consists primarily of acquisitions from descending passes of the satellites starting in 1992. We selected pairs of images covering our study sites based on the following criteria: (1) Spatial baselines (separation between orbits) of <100 m to minimize geometric decorrelation and errors due to the

Table 1. Summary of Processed Interferograms[a]

Fault	Orbits	Dates	Time Span, years	P_baseline, m	Comments
Riganpei Co	6734–17966	29 Oct 1992 to 27 Sep 19 1998	5.91	−6.4	
Riganpei Co	6233–20972	24 Sep 1992 to 25 Apr 1999	6.58	−54	miss lines
Riganpei Co	6233–21974	24 Sep 1992 to 4 Jul 1999	6.77	−25	poor cohr
Riganpei Co	6734–15962	29 Oct 1992 to 10 May 1998	5.53	−47	poor cohr
Riganpei Co	8237–20471	11 Feb 1993 to 21 Mar 1999	6.11	−66	poor cohr
Gyaring Co	6920–17150	11 Nov 1992 to 1 Aug 1998	5.72	48.9	
Gyaring Co	5918–24799	2 Sep 1992 to 12 Apr 1996	3.61	23.2	
Gyaring Co	7421–20657	16 Dec 1992 to 1 Aug 1998	6.29	−44.3	
Gyaring Co	6190–17923	21 Sep 1992 to 24 Sep 1998	6.00	37	poor cohr
Lamu Co	7092–21831	23 Nov 1992 to 24 Jun 1999	6.58	−29.8	
Lamu Co	5360–21602	25 Jul 1992 to 8 Jun 1999	6.87	47.2	
Lamu Co	4587–21831	1 Jun 1992 to 24 Jun 1999	7.06	−69.3	miss lines
Lamu Co	7364–17594	12 Dec 1992 to 1 Sep 1998	5.71	−76.4	poor cohr

[a]Interferograms with poor coherence or too many missing lines have not been used.

topography [*Zebker and Goldstein*, 1986]. (2) Image pairs with temporal baselines of more than 3 years to maximize the deformation signal in the data. Use of pairs with long temporal baselines was possible as the dry conditions prevailing in central Tibet help to preserve the radar phase coherence over long time periods. All available data meeting these criteria were processed, and for this study single interferograms are used in the fault slip inversion for each track based on the level of coherence retained. In some cases, selected pairs could not be used to extract a meaningful signal because of missing lines or bad coherence (Table 1).

[7] The raw SAR data were processed into interferograms averaged to four looks using the radar processing software, repeat orbit interferometry package (ROI_PAC) developed at the Jet Propulsion Laboratory, California Institute of Technology [*Rosen et al.*, 2004]. We used the two-pass approach and removed the topographic component of the interferometric phase using the 90 m Shuttle Radar Topography Mission (SRTM) digital elevation model. The topographic phase simulation and first flattening of the differential phase were based on the ERS satellites precise reconstructed orbits (PRC) provided by ESA. Typical errors in the PRC orbit data (~30 cm in three components) often result in a small phase ramp across the scene, which we removed by reestimating the interferometric baseline using the phase simulated from the digital elevation model. The phase unwrapping was performed using the default approach in ROI_PAC, which leaves isolated areas of coherent phase not unwrapped. Such disconnected areas were manually connected to the main unwrapped area by estimating the 2π phase ambiguity between them.

[8] In SAR interferometry data, phase decorrelation may be caused by seasonal precipitation or freeze-thaw cycles changing the scattering properties of the imaged surface [*Rosen et al.*, 2000; *Zebker and Vilasenor*, 1992]. In Tibet, interferograms made with summer scenes sometimes showed decorrelation in mountains probably due to snow coverage and interferograms made with winter scenes generally produced better results. However, despite the low coherence observed in some of the scenes, the spatial coverage of the unwrapped phase was dense enough to image the surface displacement field near active faults.

2.2. Tropospheric Phase Correction

[9] It is often observed that after the topographic component is removed from the interferometric phase, the residual phase still includes a signal that mimics the topography. This is attributed to the phase propagation delay through the wet troposphere [*Hanssen*, 2001]. Because the thickness of the tropospheric layer decreases as the surface topography increases, any change in water vapor content in the troposphere between the two epochs of image acquisition results in a differential phase delay correlating positively or negatively with the topography. This signal is an additional source of error, which in some cases can limit our ability to detect the deformation signal in the phase data.

[10] To reduce this error, we use an empirical correction method proceeding as follows. We first estimate a coefficient of proportionality between the local topography and the interferomeric phase using a correlation window of 5km x 5km. If this coefficient shows little variation throughout the scene, it is an indication of stable atmospheric conditions at epochs of data acquisitions and the correction is calculated at each pixel by scaling the elevation by the coefficient previously determined. In scenes where the coefficient varies greatly, the tropospheric error could not be estimated reliably, or is simply too small and no correction was applied. We used this approach to correct two interferograms that cover the Gyaring Co fault (section 3.2.1).

[11] We note that weather fronts and storms may produce phase delay patterns that do not correlate with the topography and cannot be estimated using the correlation between elevation and phase. In absence of ancillary data to map the precipitable water vapor in the atmosphere at the times of data acquisition, there is no way to directly estimate this error. We rely on the consistency of the observed signal along the fault length and comparison made between independent interferograms to show that the phase signal observed across the active faults is not of atmospheric origin. However, the high elevation and relatively dry climate of central Tibet generates atmospheric turbulence that produces a signal that is relatively small compared to the static tropospheric signal, as shown by the spatial stability of the phase over flat areas away from the active faults.

3. InSAR Observations and Fault Model Adjustment in the Dong Co Conjugate Fault System

[12] In this section we focus on the Dong Co conjugate fault system and on the method used to estimate the fault slip rate and locking depth by adjusting a model to the observed surface displacement. In particular, we discuss the error in the data and the resulting error on the model para-

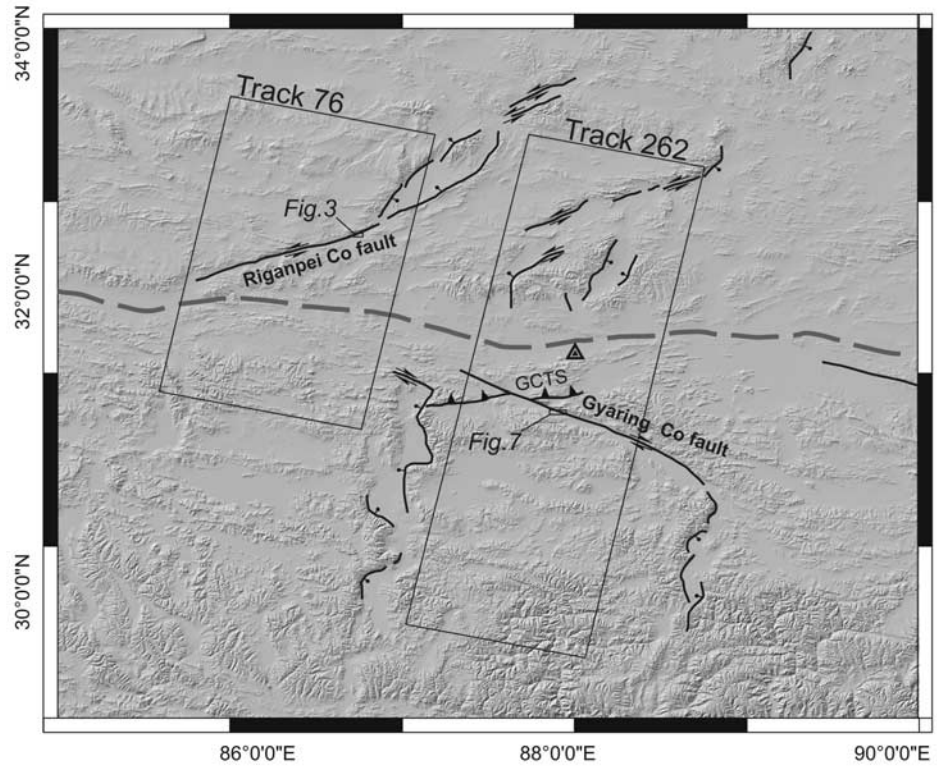

Figure 2. (a) Shaded relief map of the area spanned by the Riganpei Co and Gyaring Co faults, and north trending rift systems. Elevation data are from the Shuttle Radar Topography Mission (SRTM). Note locations of Figures 3 and 7. Faults are traced in black. Arrows indicate strike-slip motion, normal faults are indicated by bar and ball on hanging wall side. Dashed line shows the approximate location of the Bangong-Nujiang suture zone. GCTS, Goman-Caibu Co thrust system. Triangle indicates the location of GPS station NYMIA [*Chen et al.*, 2004]. See Figure 1 for location.

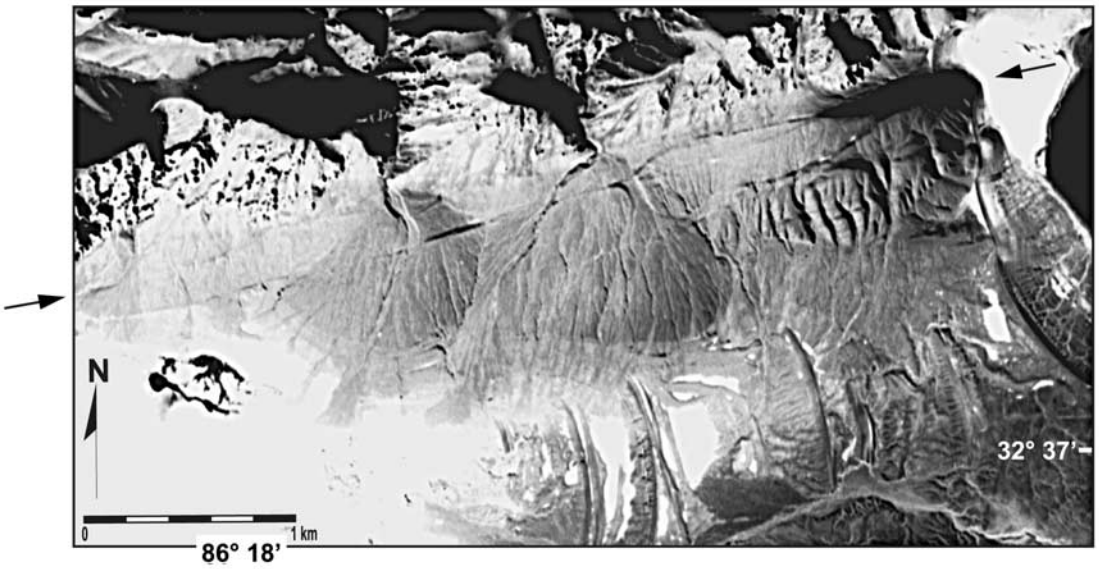

Figure 3. CORONA satellite image of the Riganpei Co fault showing offset alluvial cones overlying regressive shorelines of adjacent lake. Offsets of alluvial fans and map pattern of active fault strands are consistent with horizontal left-lateral movement on fault. See Figure 2 for location. Modified from *Taylor et al.* [2003].

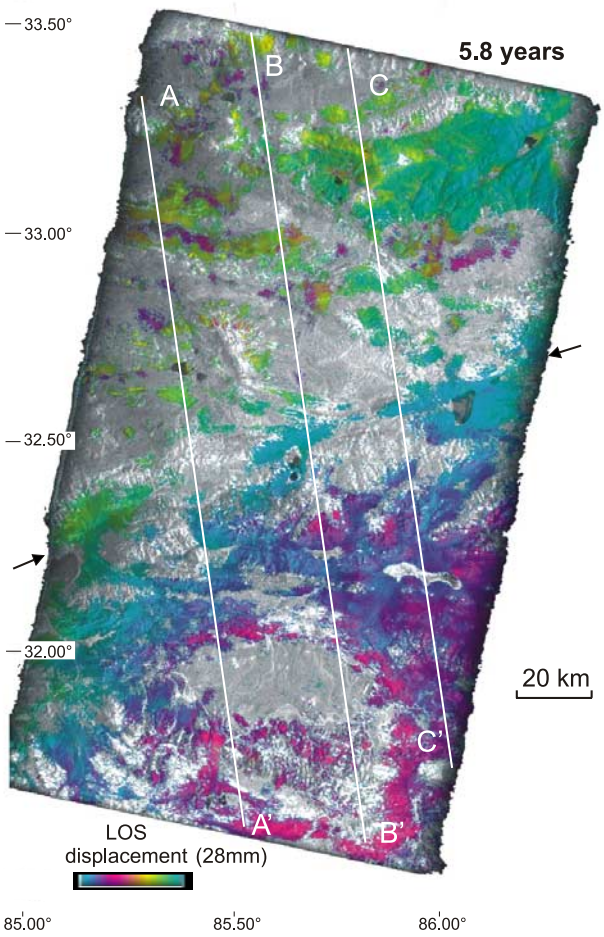

Figure 4. Interferogram of the RPCF area spanning 5.8 years (see Table 1). Colors show the interferometric phase. One color cycle corresponds to 28 mm of phase change along radar line of sight (LOS). Intensity is radar amplitude image. Gray areas are where phase coherence is low and have been masked before phase unwrapping. White lines indicate location of profiles shown in Figure 5. Arrows indicate location of the Riganpei Co fault. See Figure 2 for location.

meters. The same method is then applied to the study of other fault systems in the subsequent sections of the paper.

3.1. Interseismic Motion Along the Riganpei Co Fault

[13] The Riganpei Co fault comprises the northern segment of the Dong Co conjugate strike-slip fault system and is a ~120 km long, left-lateral fault in central Tibet with a ~N71°E strike (Figure 2). The fault connects with the central segment of the Yibug Caka rift system to the north, and with small west dipping normal faults that connect with the Bangong-Nujiang suture zone to the south (Figure 2). The magnitude of the total displacement along the entire fault system is estimated to be between 7 and 14 km, from the left separation of two north dipping thrust faults and the restoration of a Mesozoic low-angle normal fault system to the north [*Kapp et al.*, 2003; *Taylor et al.*, 2003]. Recent disruption and offset of an alluvial fan complex located along the north shore of Riganpei Co is consistent with left-lateral horizontal motion along this structure (Figure 3) [*Taylor et al.*, 2003].

[14] We analyzed SAR data acquired over track 76, which covers the Riganpei Co fault. The interferogram in Figure 4 spans a time interval of 5.8 years from 29 October 1992 to 27 September 1998. The interferometric phase field shows a range increase from south to north with a zone of concentrated deformation at the Riganpei Co fault (Figure 4). The 200-km-long profiles oriented perpendicular to the Riganpei Co fault reveal that the deformation signal corresponds to 5 mm of phase change along the radar line of sight (LOS) distributed over a 30- to 40-km-wide zone across the fault (Figure 5). North and south of this zone, the phase field is flat with a small tilt of ~0.4 mm (100 km)$^{-1}$ that we attribute to orbital error. On these profiles, we observe no correlation between the phase signal and the local topography suggesting that any error due to the phase delay in the troposphere is negligible (Figure 5) [*Zebker et al.*, 1997]. Another source of error contributing to the phase noise involves hydrologic processes and the freeze-thaw cycle of the soil. These effects are more likely to be observed in basins where soils can develop, rather than in areas of rugged and rocky surfaces in mountainous terrains. However, the relatively flat phase profiles observed across a variety of terrains and topography (Figure 5) indicates that these errors are small. We therefore interpret the phase change occurring within 20 km from the fault as ground displacement produced by creep at depth on a fault plane locked at shallow depth.

3.2. Estimating Fault Model Parameters and Associated Errors

[15] To fit a fault model to the observed surface displacement, we must relate the surface displacement field to the range change it produces in the InSAR image. A three-dimensional displacement vector $V = (e, n, u)$ in the local east north up reference frame, is projected along the radar LOS as

$$R = [n \sin(\alpha) - e \cos(\alpha)]\sin(\theta) + u \cos(\theta) \quad (1)$$

where α is the azimuthal heading of the satellite and θ is the local incidence angle of the radar LOS direction in a right-looking antenna configuration. If we assume that the ground displacement is horizontal, parallel to a fault with strike β, and of magnitude V, the displacement vector is $\mathbf{V} = V(-\sin\beta, \cos\beta, 0)$ and the corresponding range change is

$$R = V\sin(\alpha - \beta)\sin(\theta) \quad (2)$$

[16] Our observations both in the field and on the satellite images indicate that the Riganpei Co fault is purely strike-slip along its central segment (Figure 3). An infinitely long, purely strike-slip dislocation, buried in an elastic half-space produces a horizontal displacement field which is parallel to its strike at any point. The magnitude of such a field at a distance x from the fault can be expressed as a function of the fault displacement D and locking depth h as [*Savage and Burford*, 1973]

$$V = D/\pi \operatorname{atan}(x/h) \quad (3)$$

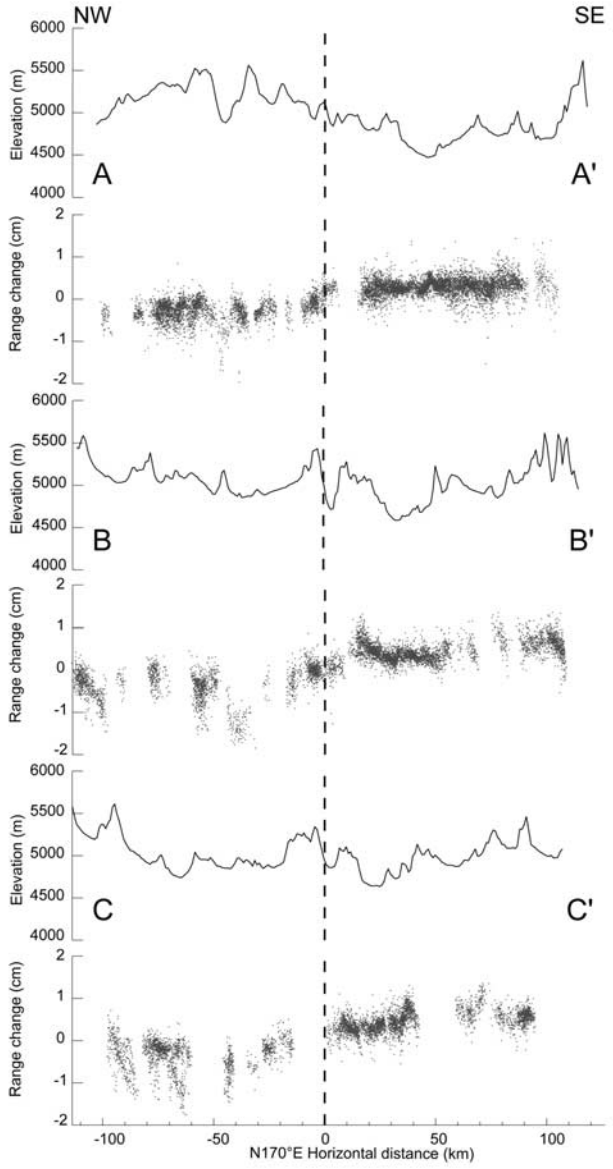

Figure 5. Colocated profiles of topography and phase change across the Riganpei Co fault. Topographic and phase profiles are generated from 4- and 40-km-wide swaths, respectively. Note absence of correlation between phase signal and topography. Phase is flat in far-field with localized strain within 40 km of the fault. See Figure 4 for profile locations.

We use the angular relationship in equation (2) and the parameterization of equation (3) to solve for the horizontal fault-parallel slip rate and locking depth using a least squares inversion.

[17] A source of uncertainty in the fault model solution is the noise in the SAR data and possible spatial variations of the ground displacement around the fault zone resulting in the scattering of the data points throughout the interferograms. In displacement profiles oriented perpendicular to faults such as those shown in Figure 5, all data points within a box of given width are projected onto the profile, emphasizing the spatial dispersion of the data. This dispersion directly contributes to the error in the fault slip solution. To estimate the fault slip rate and locking depth and associated errors, we proceed in four steps. First we estimate the data dispersion profile by computing the RMS scatter of the data in a 10-km-long sliding window along the profile axis. The standard error of the data (σ) is taken to be the mean data scatter along the profile. A weighting function is also computed from the reciprocal of the data scatter. Second, a model function of the form

$$F = D/\pi \text{ atan } (x/h) + ax + b \tag{4}$$

is adjusted to the data using a nonlinear least squares approach and the weighting function defined in the previous step to estimate a first set of model parameters (D, h, a, b). The adjustment is made using the Interactive Data Language (IDL) CURVEFIT procedure, which iteratively adjusts the parameters of a nonlinear function to a set of data points until the chi-square variation reaches a given threshold. This adjusted function includes the fault model of equation (3) and a linear trend to take into account residual orbital errors that may result in a small tilt in the projected data. Third, we estimate the trade-off between fault slip rate and locking depth by computing the model data quadratic misfit over a range of values for the slip rate and locking depth, keeping the linear coefficients (a and b) fixed to their estimated values. Fourth, because the slip rate on the fault is derived from the distance between the flat, far-field sections of the data profile on either sides of the fault, the width of the error interval on the slip rate is directly related to the data scatter along the profile. We fix the width of the interval error on the fault slip rate to 2σ and search the contour in the misfit plot that subtends a 2σ interval on the slip rate axis (Figure 6 inset). This elliptical contour defines the minimum and maximum values for the fault slip rate and locking depth (Figure 6 inset). Note that the interval bounds are not symmetrical with respect to the value that minimizes the misfit function, which we discuss below.

[18] The contour in the model data misfit plot in Figure 6 inset highlights the trade-off between slip rate and locking depth and indicates that the data do not place tight constraints on the value of the locking depth. This result may be biased by the fact that the data points constraining the locking depth are the points defining the maximum displacement gradient across the fault and the misfit is computed for the entire profile length. The weight of the steep gradient section of the profile is relatively small in the overall misfit calculation.

[19] An additional source of error on the slip rate and locking depth may be due to an erroneous estimate of the linear slope in adjusting function F to the displacement data. To estimate the sensitivity of the slip rate solution to errors on the profile tilt, we reestimate the slip rate by a nonlinear fit, by varying the profile tilt over the $[a - 2\ \sigma/L, a + 2\ \sigma/L]$ interval and keeping all other parameters constant. Because the phase field is flattened in the interferometric baseline reestimation procedure, residual tilts in the profile reflect spatial variance in the data and not original errors in the knowledge of the satellite orbits. We therefore assume that the possible errors on the tilt value do not exceed 2σ divided by the profile length (L). We observe that the estimated slip rate is increased when the tilt increases the overall slope of

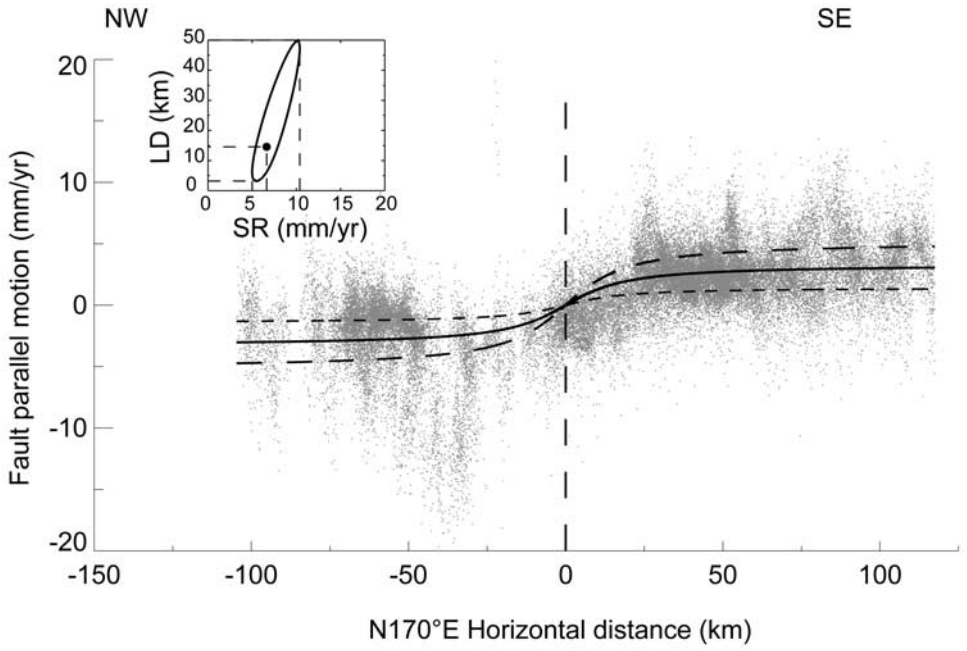

Figure 6. Surface movement obtained with elastic dislocation model (solid line) fit to InSAR data (gray dots) across the Riganpei Co fault. Note that line-of-sight displacement data have been projected into fault-parallel velocity assuming horizontal strike-slip motion on fault (see text). Solid line is model obtained with optimal slip rate and locking depth, and dashed lines indicate model using maximum and minimum slip rates allowed in error interval. Vertical dashed line is fault location. Inset shows a contour and location of minimum of misfit between data and model in slip rate (SR) and locking depth (LD) parameter space (see text).

the profile, and is decreased when it decreases the overall slope of the profile. The newly estimated bounds for the slip rate estimated using profile tilts spanning the $a \pm 2\sigma/L$ interval are compared to those estimated from the contour in Figure 6 inset and the most conservative values are assumed. Table 2 summarizes the results of this analysis.

[20] For the profile shown in Figure 6, the model slip rate and the locking depth that best fit the data are 6.6 mm yr^{-1} and 15 km, respectively. The standard error on the projected data is σ = 2.7 mm yr^{-1} yielding error intervals of 5–10 mm yr^{-1} and 4–50 km on the slip rate and locking depth, respectively. The extreme values for the slip rate obtained with tilts varying over a range of $\pm 2\sigma/L$ around the nominal value are 3.4 and 11 mm yr^{-1}. We therefore retain the conservative interval of 3.4–11 mm yr^{-1} for the slip rate on the Riganpei Co Fault (Table 2).

3.2.1. Gyaring Co Fault

[21] The 250-km-long Gyaring Co fault is geomorphically expressed as a linear valley that trends ~N70°W in the northern Lhasa terrane (Figures 1, 2, and 7). Its northern end merges with the southern end of the Riganpei Co fault along the Bangong-Nujiang suture, and its southern end is linked with the north trending Pum-Qu-Xainza rift (Figures 1 and 2). This relationship suggests that the Gyaring Co and Riganpei Co faults may form a conjugate strike-slip set, which would require a comparable magnitude of displacement across the two faults assuming a uniaxial compression field. Assuming planar fault geometries, *Taylor et al.* [2003] calculated 12 ± 4 km of right-slip and about 100 m of dip-slip motion along the Gyaring Co fault by restoring an intersection line made between the east striking Goman-Caibu Co thrust systems, and an underlying Tertiary unconformity that is cut by the north dipping thrust fault (Figure 2). Field and satellite observations along the trace of the Gyaring Co fault suggest recent activity with the fault trace cutting Quaternary alluvial fans and terrace risers, and locally forming pressure ridges and sag ponds (Figure 7). At the southeastern end of the Gyaring Co fault, *Armijo et al.* [1989] documented evidence for a

Table 2. Summary of Fault Model Results[a]

Fault	Figure	Orbits	Model Slip Rate, mm yr^{-1}	Error Interval, mm yr^{-1}	Model Locking Depth, km	Error Interval, km	Data Noise, mm yr^{-1}	ProfileTilt, mm yr^{-1} 100 km^{-1}	Minimum Tilt, mm yr^{-1} 100 km^{-1}	Maximum Tilt, mm yr^{-1} 100 km^{-1}	Conservative Error Interval mm yr^{-1}
RPF	6	6734–17966	6.6	4.9–10.3	14.5	4–50	2.69	0.2985	−0.540	−0.056	3.4–11
GYF	11a	6920–17150	14.5	12.2–18.1	23	13–41	2.93	0.1494	−0.469	−0.188	10.0–19.0
GYC	11b	5918–24799	13.4	10.8–18.3	27	15.5–50	3.76	0.3524	−0.035	0.7401	7.8 –20.8
GYF	11c	7421–20657	12.3	10.2–15.2	24.3	13.4–38	2.55	0.9796	−1.289	−0.669	7.5–17.1
LCF	15b	7092–21831	2.1	1.4–3.3	3	0.1–22	0.9	0.2961	0.443	−0.148	1.0–3.3
LCF	15c	5360–21602	4.1	2.2–7.1	5.8	0.1–31	2.5	1.6808	1.173	2.188	0.1 –8.0

[a]Data noise is computed as the RMS scatter along a 10-km-long sliding window.

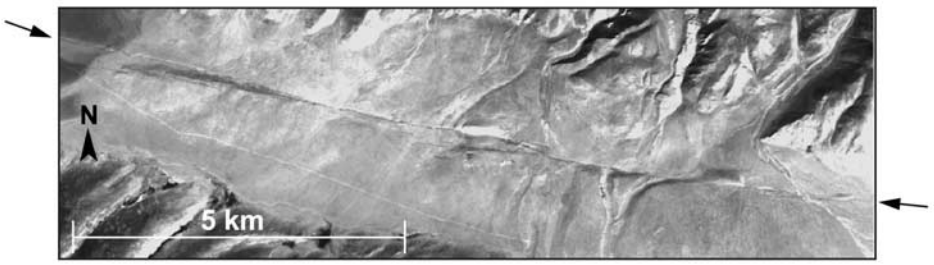

Figure 7. CORONA satellite image of the Gyaring Co fault (arrows) showing fault scarps, pressure ridges, and offset and beheaded streams. Changes in fault strike produce an extensional jog (center) and compressional jog (right), which are consistent with right-slip motion on fault. See Figure 2 for location.

recent rupture near Xianza that they attribute to an earthquake of possible M7.

3.2.2. Interseismic Motion Along the Gyaring Co Fault

[22] We analyzed three independent interferograms covering the Gyaring Co fault from a descending orbit along track 262 (Figure 8). Two of them are constructed with four ERS frames and cover a ~400-km-long section of track 262. One of the interferograms includes only two frames because data were missing from orbits 7421 and 20657 and is ~200 km long (Figure 8).

[23] For the two long interferograms shown in Figures 8a and 8b we noticed a clear correlation between the phase and small variations in the topography. This topographic signal in the residual phase is due to variable tropospheric conditions with consistent stratification existing between the two epochs of data acquisition for a given interferometric pair. We used the empirical approach described in section 2

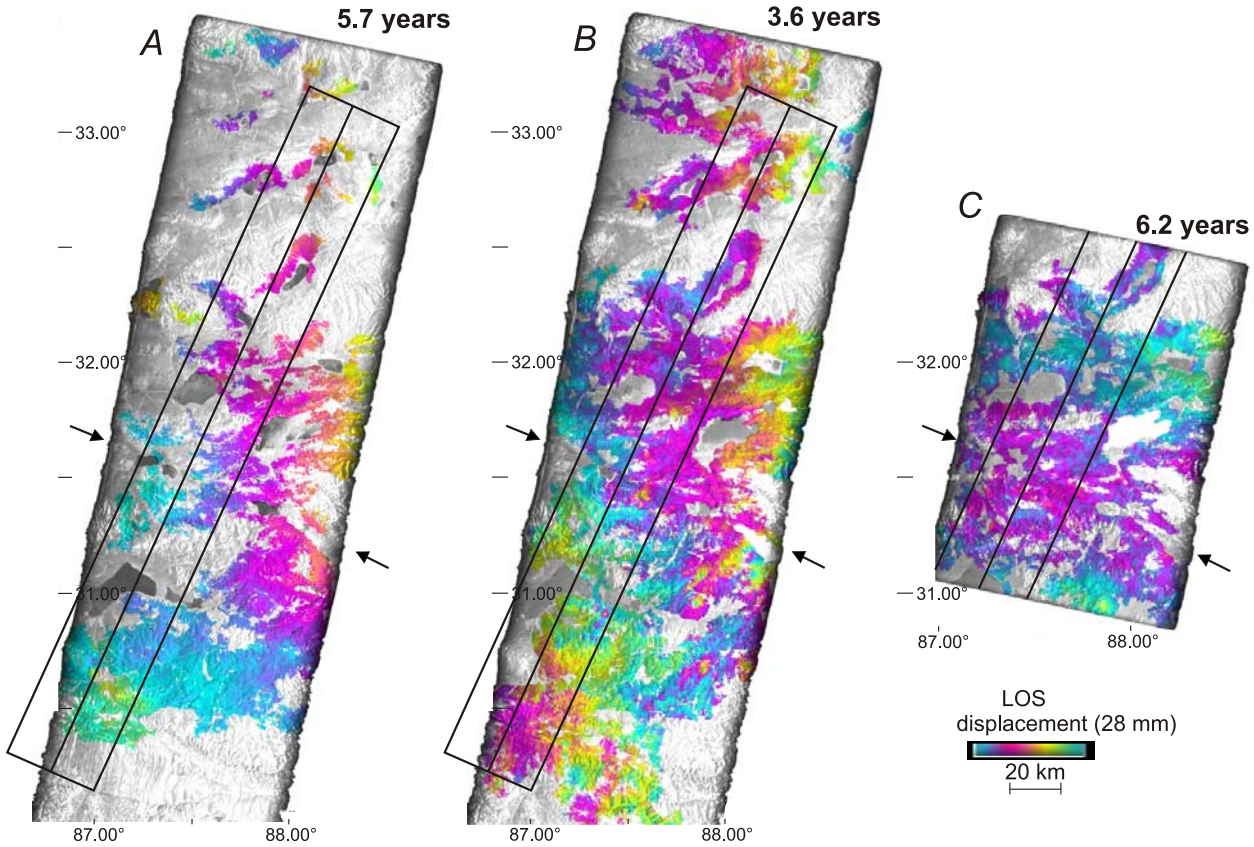

Figure 8. Interferograms of Gyaring Co fault area spanning (a) a 5.7-year time period (orbits 6920–17150), (b) 3.6-year time period (orbits 5918–24799), and (c) 6.2-year time period (orbits 7421–20657). Colors are as in Figure 4. Black box indicates sampling area for the profiles shown in Figures 10 and 11. See Figure 2 for location.

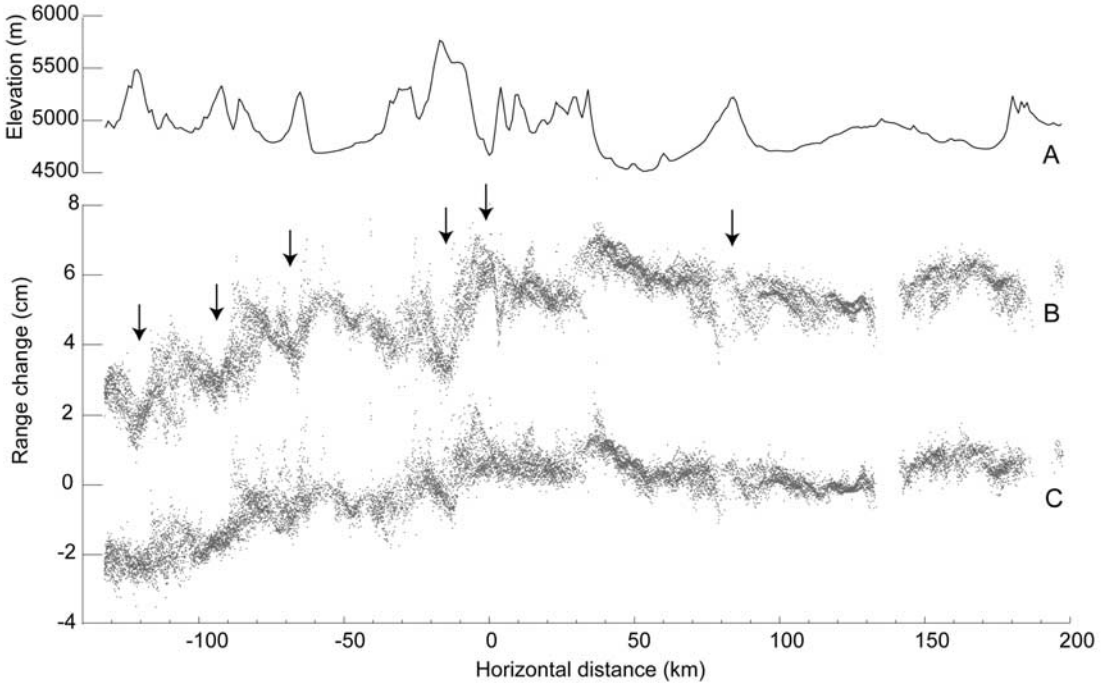

Figure 9. Colocated profiles of (a) topography, (b) observed LOS phase change, and (c) LOS phase change after troposphere correction (see text) across Gyaring Co fault. Data are from interferogram in Figure 8a (orbits 6920–17150). See Figure 8 for profile locations. Topographic and phase profiles are generated from 4- and 10-km-wide swaths, respectively. Note correlation between elevation and observed phase (arrows) related to phase propagation delay through troposphere in profile in Figure 9b. Profile in Figure 9c is corrected for troposphere effects and shows no clear correlation with topography.

to reduce the effects of the troposphere in these data. Figures 9a and 9b illustrate the correlation between the observed phase and the topography along a ~300-km-long profile across the Gyaring Co fault. For these data we estimated a topography dependant signal of approximately 3 and 4 rad km^{-1} for the two interferograms of Figures 8a and 8b, respectively. After correction, the small wavelength features correlating with the local topography are not clearly visible in the phase (Figure 9c).

[24] To determine the current slip rate on the Gyaring Co fault, we used the same approach as for the Riganpei Co fault (Section 3.2). The function fit was done with the corrected data keeping only the data points within 100 km from the fault to avoid areas where the signal could be influenced by other active structures. For example, near +150 km along the profiles in Figure 10 the sampling area covers the Bangong-Nujiang suture zone and the active north trending rift systems that may influence the phase there. Similarly, the two long profiles consistently show an apparent range increase south of –100 km on the profiles in Figures 10a and 10b, although this signal cannot be associated with any known active structure south of the Gyaring Co fault. The 200-km-long interferogram (Figure 10d) spans the largest time interval of the three we analyzed on the Gyaring Co fault. Unfortunately, the missing frame to the south makes the interferogram too short to capture the far-field displacement beyond 50 km south of the Gyaring Co fault. However, the curvature of the phase in the profile perpendicular to the fault in Figure 10d is consistent with the signal observed in the other two profiles (Figures 10b and 10c) and is consistent with right-lateral shear across the fault zone.

[25] We estimated the slip rate and locking depth of the fault using the 3 profiles independently. The optimal fault parameters are consistent with a right-lateral fault slipping at a rate between 12.3 and 14.5 mm yr^{-1} for the phase profiles in Figure 11. The mean data dispersion on these profiles ranges between 2.5 and 3.7 mm yr^{-1} yielding an error interval on the slip rate of 10.2–18.3 mm yr^{-1}. The corresponding locking depth varies between 23 and 27 km (Table 2). After investigating the effect of varying the tilt in the profile, the conservative bracket for the error on the fault slip rate became 7.5–20.8 mm yr^{-1}. The slip rate determined here for the Gyaring Co fault is comparable to the long-term slip rate of ~15 mm yr^{-1} estimated by *Armijo et al.* [1989] on the Jiali fault, another segment of the KJFZ, ~500 km to the east.

4. InSAR Observations Along the Bue Co Conjugate Fault System

[26] The Bue Co conjugate fault system is located ~400 km to the west of the Dong Co conjugate system and consists of two fault segments that intersect near Bue Co (Figures 12 and 13). The Bue Co fault strikes ~N70°E and forms the northern segment of the strike-slip conjugate system. The Bue Co fault is a left-lateral strike-slip fault with a small dip-slip component (Figure 12). This interpre-

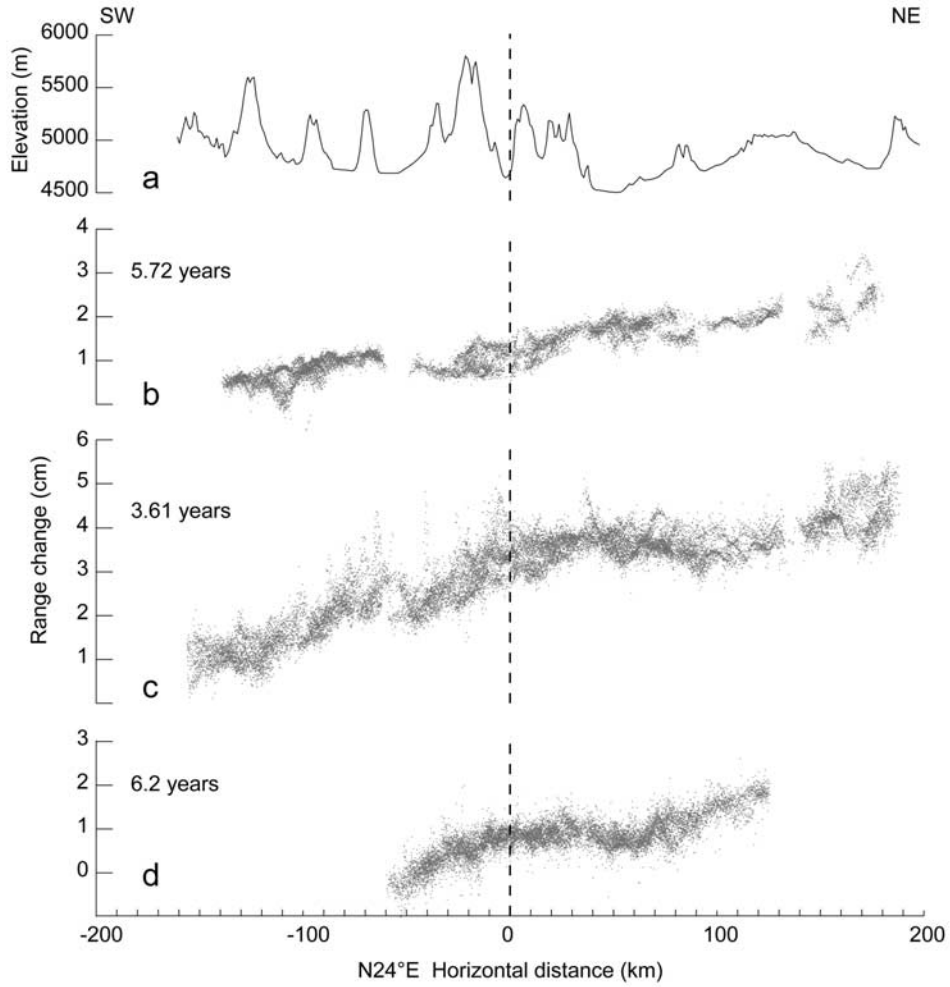

Figure 10. Colocated profiles of (a) topography and (b–d) LOS phase change after correction for troposphere phase delay (see text) across Gyaring Co fault. Topographic and phase profiles are generated from 4- and 10-km-wide swaths, respectively. Note relatively flat profile in far-field with curvature localized within ~60 km of the fault. Profile in Figure 10d is shorter due to missing data in south. See Figure 8 for profile locations.

tation is based on a ~25-km-long and ~7-km-wide crescent-shaped basin that is bounded on its east side by the Bue Co fault. This basin geometry results from left-slip motion along a releasing bend of the fault. The active nature of the fault is suggested by its trace cutting several alluvial fans [*Taylor et al.*, 2003]. The magnitude of left-lateral motion along the Bue Co fault is 12 ± 3 km, as estimated from the left separation of a Permian limestone unit [*Cheng and Xu*, 1987] observed in Landsat 7 imagery (Figure 13).

[27] Only one interferogram (track 205) in our data set covers the Bue Co fault (Figure 14a). This interferogram spans 6.8 years and unfortunately does not have good coherence over the Bue Co fault area, preventing us from observing any ground displacement across the fault (Figure 14a).

[28] The Lamu Co fault forms the southern segment of the Bue Co conjugate strike slip fault system. The fault strikes ~N55°W and consists of two right-stepping segments, overlapping along the sides of a prominent pull-apart basin (Figures 12 and 13). This geometry implies that the Lamu Co fault is a right-slip structure. The northern fault segment strikes N50°W, is ~45 km long, and truncates Jurassic volcanic strata displaying 17 ± 5 km of right-lateral separation (Figure 13). The southern segment of the Lamu Co fault, also visible in the Landsat 7 image to the south of the pull-apart basin, exceeds 95 km in length, and truncates east striking Jurassic strata. The magnitude of displacement along this fault segment is unknown.

[29] Two adjacent interferograms (tracks 205 and 434) cover the Lamu Co fault (Figures 12 and 14). Both interferograms cover a period of approximately 6 years. The phase coherence however, is quite poor in the western interferogram compared to the coherence of the eastern one. This may be related to the season during which the acquisitions were made (23 November 1992 and 24 June 1999), since snow precipitation is likely during late November in central Tibet. In the vicinity of the Lamu Co fault, both interferograms have coherent phase, although the level of noise is greatest in the interferogram covering track 205. This is apparent on the profiles made perpendicular to the Lamu Co fault (Figure 15c). Both profiles of the phase

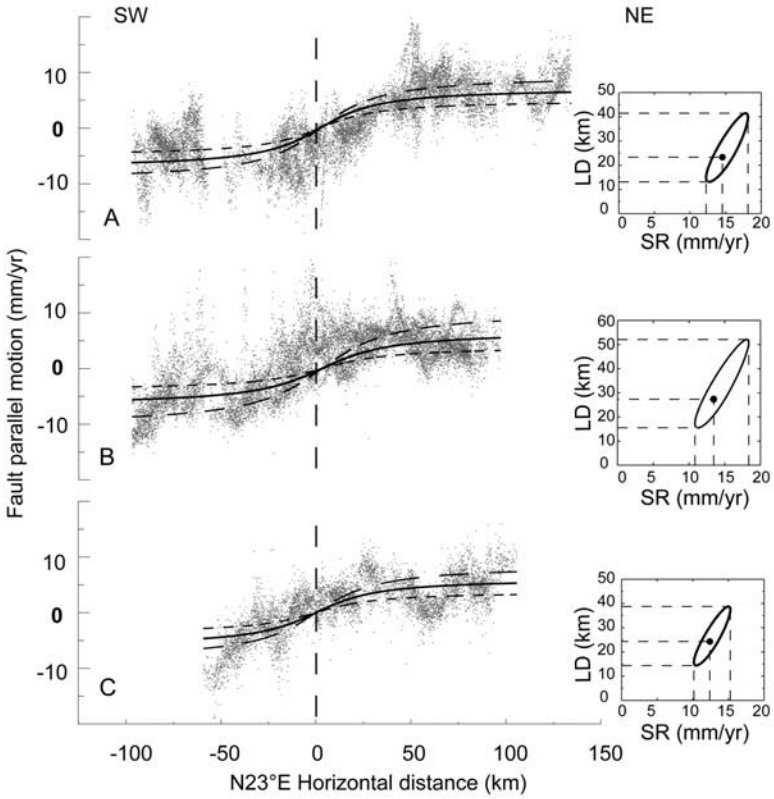

Figure 11. Same as Figure 6 for three independent interferograms from track 262 across the Gyaring Co fault spanning (a) 3.6 years, (b) 5.7 years, and (c) 6.29 years. Profiles of fault-parallel displacement are generated from a 20-km-wide swath. See Figure 8 for profile locations.

indicate a consistent direction of displacement across the Lamu Co fault, with the north side of the fault moving toward the satellite with respect to the southern side. If we assume that the displacement along the fault is horizontal, the observed range change is consistent with a right-lateral direction of slip along the Lamu Co fault. The topographic profile colocated with the phase profiles do not show any large size feature at the fault, which could potentially corrupt the displacement signal through varying tropospheric phase delay (Figure 15). We are therefore confident that the observed signal is related to creep at depth along the fault.

[30] Least squares fits of the fault model of equation (4) to the phase data in Figure 15, indicate a horizontal slip rate for the Lamu Co fault of 2.1 and 4.1 mm yr^{-1}, respectively. The data noise is larger in the Figure 15c profile than in the Figure 15b profile, as expected given the overall low coherence in the interferogram of track 205 (Figure 14). The apparent slip rate determined with the second profile is 4.1 mm yr^{-1}, higher than the value of 2.1 mm yr^{-1} estimated with the first profile, but the error associated with the higher slip rate is also larger (Table 2). The optimal locking depths for the two profiles are very shallow although the associated error would allow locking depths of up to 30 km. When investigating the effect of varying the tilt of the data profiles on the fault slip rates, the combined error interval becomes 0.1–8 mm yr^{-1} (Table 2). If we take the weighted mean between the two slip rate estimates (with weights based on conservative error intervals), our preferred slip rate estimate for the Lamu Co fault is 2.6 +1.6 −0.9 mm yr^{-1}.

5. Discussion

5.1. Tectonic Regime in the Central Tibet Conjugate Strike-Slip Fault System

[31] *Armijo et al.* [1989] described the details of active structures in the Lhasa terrane and proposed that the eastward extrusion of the Qiangtang terrane, relative to the Lhasa terrane was accommodated along a zone of decoupling defined by the en echelon KJFZ. The Qiangtang block was viewed as relatively undeformed as the right-lateral faults of the KJFZ appeared to transfer slip into the north trending rift valleys to the south, resulting in distributed east west extension of the Lhasa terrane.

[32] In that model, the KJFZ combines with the Altyn-Tagh and Kunlun fault systems to the north to control the extrusion of the Qiangtang block, squeezed between the Tarim Basin to the north, and the Lhasa block to the south [*Armijo et al.*, 1989]. On the basis of previous field studies [*Taylor et al.*, 2003] and the present InSAR results, we expand upon the observations of *Armijo et al.* [1989] and include in the fault zone the northeast striking left-slip faults of the southern Qiangtang to form the east trending central Tibet conjugate strike-slip fault zone.

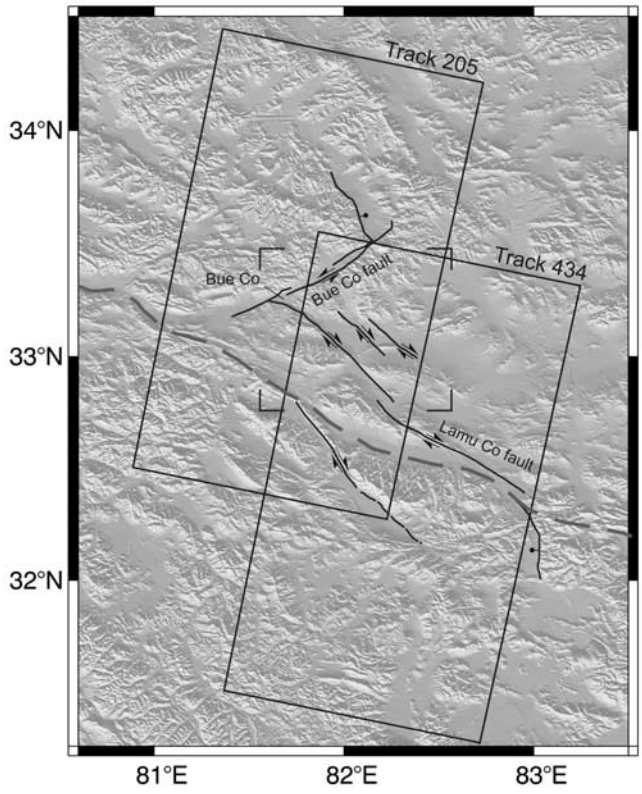

Figure 12. Shaded relief map of the western Tibet sites. Boxes indicate locations of ERS satellite tracks shown in Figure 14. Brackets indicate area covered by Figure 13. Fault symbols are same as in Figure 2. Dashed, gray line is the approximate location of the Bangong-Nujiang suture zone. See Figure 1 for location.

[33] The slip rates on the faults forming the Dong Co conjugate strike-slip system can be used to determine the strain regime currently prevailing in central Tibet. Given the geometry of the system (Figure 2), the 6 mm yr^{-1} of left-lateral slip on the Riganpei Co Fault and a conservative rate of 11 mm yr^{-1} of right slip on the Gyaring Co Fault imply roughly ~5 mm yr^{-1} of shortening in a N10°E direction (pure shear) over-imposed on a ~N100°E, simple shear regime accommodating ~6 mm yr^{-1} of right-lateral shear between the Lhasa and Qiangtang blocks. This means that part of the right-lateral slip observed on the Gyaring Co fault is due to the simple shear on the conjugate fault system over a ~60-km-wide zone and not entirely related to the eastward movement of a rigid Qiangtang block. Using GPS data, *Chen et al.* [2004] constructed a deforming block model of the Tibetan Plateau to derive deformation rates of the central Tibetan crust. Their model identified a region of differential right-lateral shear in the vicinity of the KJFZ estimated to be accommodating ~7.5 mm yr^{-1} of right-lateral shear, in general agreement with our results. Because the analysis of *Chen et al.* [2004] used widely spaced GPS stations, concentrated zones of deformation were not identified. Interestingly, while the north south shortening observed in the GPS data appears broadly distributed throughout the north south extent of the plateau, the simple shear deformation in central Tibet appears to be limited over a ~60-km-wide zone across the conjugate fault belt.

5.2. Locking Depth

[34] Although the dispersion in the SAR data results in large uncertainties in the determination of the locking depth on faults in central Tibet, InSAR data shows that elastic deformation is generally localized within a 30- to 60-km-wide zone along the trace of known active faults, a feature of the deformation field that is not visible in the campaign GPS data currently available in Tibet [*Wang et al.*, 2001]. Assuming uniform elastic properties of the upper crust, the width of the observed deformed zones is generally consistent with faults locked down to a depth of 16–25 km. An exception is the narrower concentration of the deformation across the Lamu Co fault in western Tibet, which under the same model assumptions would indicate a shallower locking depth of 3–5.8 km.

[35] If the locking depths in central Tibet are indeed 25 km or less, it would be consistent with observations of the regional seismicity [*Langin et al.*, 2003; *Molnar and Chen*, 1983; *Molnar and Lyon-Caen*, 1989]. Other observations that are generally consistent with a seismogenic depth less than 25 km include "bright spots" imaged in seismic reflection data [*Brown et al.*, 1996], midcrustal low velocities from receiver function analysis [*Owens and Zandt*, 1997], highly conductive layers imaged at midcrustal levels using magnetotelluric data [*Wei et al.*, 2001], and relatively thin effective elastic thicknesses in southern Tibet [*Masek et al.*, 1994].

5.3. Current and Long-Term Slip Rates on Faults in Central Tibet

[36] The slip rates we determined for individual faults in the central Tibet fault zone are generally lower than the rates estimated by GPS [*Bendick et al.*, 2000; *Shen et al.*, 2001; *Wallace et al.*, 2004] or InSAR [*Lasserre et al.*, 2001; *Socquet et al.*, 2005] for the central section of the Altyn Tagh fault bordering Tibet to the north. While the current slip rate along the Karakoram fault is not well constrained, it appears to have a geodetic slip rate that ranges between 3 and 11 mm yr^{-1} based on GPS and InSAR data [*Banerjee and Bürgmann*, 2002; *Jade et al.*, 2004; *Wright et al.*, 2004], a range comparable to the range of rates we estimated for the central Tibet faults.

[37] However, the central Tibet strike-slip faults have accumulated less slip in the Cenozoic than the Altyn Tagh fault by an order of magnitude [*Cowgill et al.*, 2003; *Gehrels et al.*, 2003; *Métivier et al.*, 1998; *Peltzer and Tapponnier*, 1988], and at least a factor of five less than the Karakoram fault [*Murphy et al.*, 2000; *Taylor et al.*, 2003]. While, the initiation age for strike-slip faults in central Tibet has not been established, their association with the north trending rift systems in the Lhasa block may be an indication of coeval development [*Armijo et al.*, 1989; *Taylor et al.*, 2003; *Yin and Harrison*, 2000]. Thus the timing of the initiation of normal faulting in Tibet may provide an estimate of the initiation age of strike-slip faulting. Geologic studies conducted along the ~north trending Yadong-gulu rift system in the Lhasa block indicate that east west extension began at ~8 Ma [*Harrison et al.*, 1995]. Using the same approach in the Qiangtang, $^{40}Ar/^{39}Ar$ cooling ages obtained on synkinematically growing muscovite from a north striking normal fault zone suggests that east west extension was active at ~13.5 Ma [*Blisniuk et al.*, 2001].

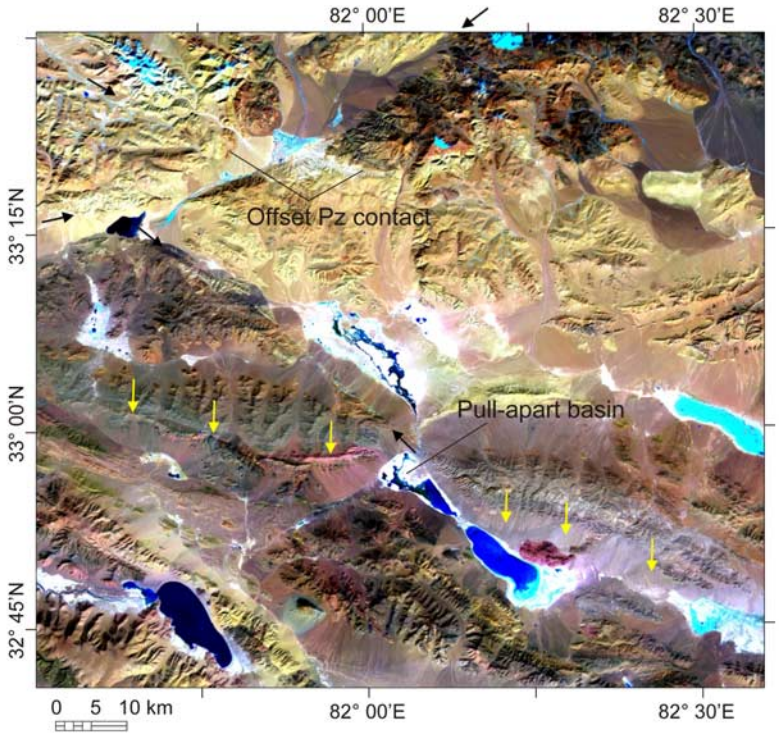

Figure 13. Color composition of Landsat bands 7, 4, and 1 covering the Lamu Co and Bue Co faults. Note dextral separation (17 km) of south directed Mesozoic thrust fault (depicted by yellow arrows) along the Lamu Co fault, and the sinistral separation (~11 km) of a Paleozoic contact along the Bue Co fault in north central part of image. Fault scarps are observed between black arrows. Northwest trending lakes in lower half of image are consistent with a pull-apart geometry along right-slip faults. See Figure 12 for location.

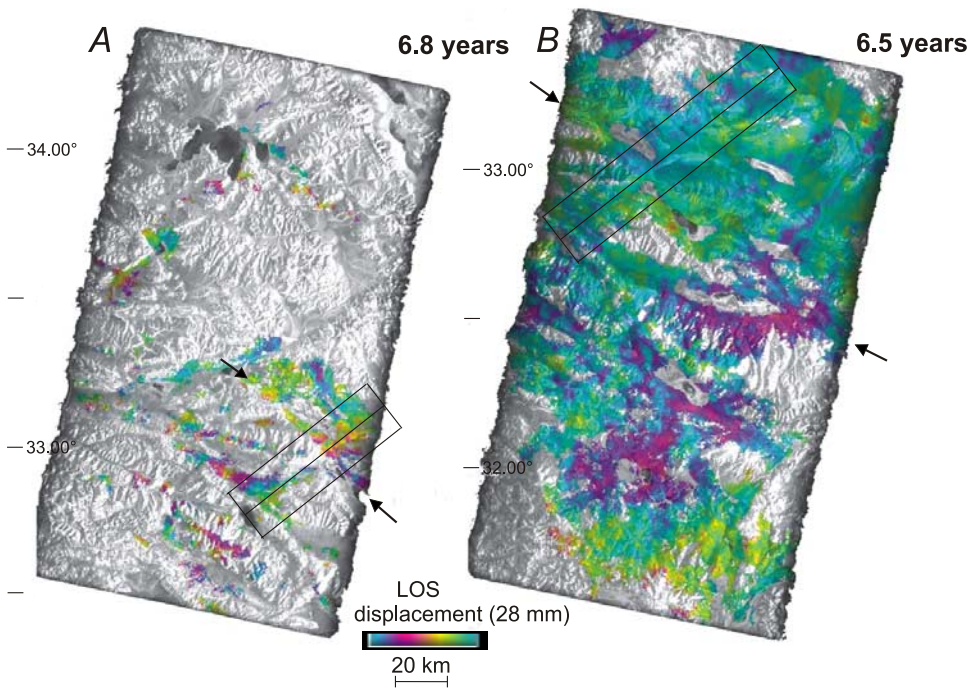

Figure 14. Interferograms covering the Lamu Co fault and spanning (a) 6.8 years (track 205, orbits 5360–21602) and (b) 6.5 years (track 434, orbits 7092–21831). Colors are as in Figure 4. See Figure 12 for location.

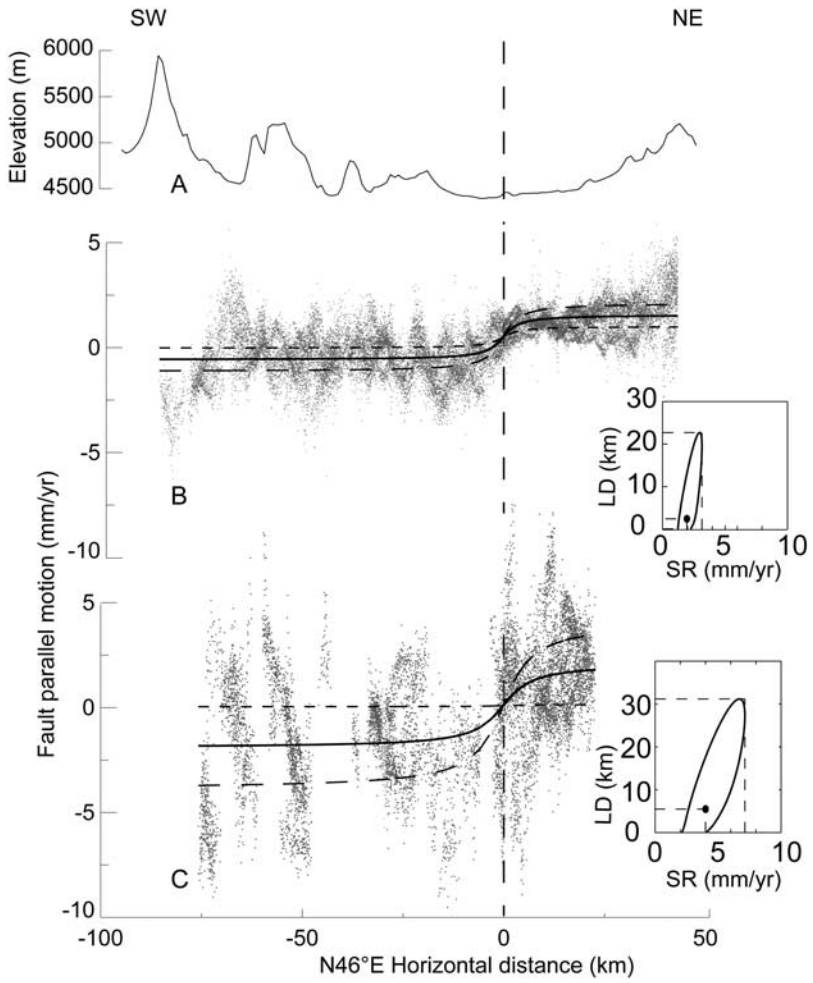

Figure 15. Same as in Figure 6 for two interferograms from adjacent tracks 205 and 434 covering the Lamu Co fault. Phase profiles of fault-parallel displacement are generated from 20-km-wide swaths. See Table 2 for estimated fault slip rates and locking depths and Figure 14 for profile locations.

Further to the east, *Lee et al.* [2003] suggest that the Jiali right slip fault was active between ~18 and 12 Ma. However, assuming a constant slip rate over the life span of the conjugate faults, even the slower slip rates determined from our InSAR analysis would only require the faults to have initiated in the past 2–3 Myr.

[38] In the Shuang Hu graben, *Blisniuk and Sharp* [2003] determined the slip rate on a range-bounding normal fault by dating offset fluvial terraces using U series dating of pedogenic carbonate rinds on cobbles collected from the terrace surfaces. Although ~north striking normal faults were studied, their results yielded a very slow cumulative slip rate of ~0.3 mm yr^{-1} for the two fault strands identified, although it was not clear if the spatially integrated slip rate across the entire fault system was determined in that study. This slip rate is extremely low over timescales of tens to hundreds of thousand years and is in marked contrast to the active and relatively higher slip rates determined in this study for the conjugate strike-slip faults of central Tibet.

[39] This discrepancy between the slip rates and magnitudes of slip determined for the conjugate strike-slip faults of central Tibet [*Taylor et al.*, 2003, this study], the apparent initiation of slip on the faults at ~8 Ma, and the slow slip rates over tens to hundreds of thousand years [*Blisniuk and Sharp*, 2003] suggests that fault slip rates in central Tibet may reflect nonsteady state behavior and that fault slip rates may have accelerated with time. Additionally, the fact that the total slip accumulated on the central Tibet faults does not match the magnitude of fault slip for the Altyn-Tagh and Karakoram faults indicates that the former faults are younger structures that are likely to be unstable over long periods of time.

5.4. Evolution of the Central Tibet Fault System

[40] The KJFZ developed as a series of en echelon fault segments at the surface at the latitude of the Bangong-Nujiang suture zone in response to the eastward movement of the Qiangtang. Within the fault zone, the deformation tends to localize along discrete strike-slip fault segments, which cut the preexisting structural fabric of the Tibetan crust. The fact that the en echelon KJFZ does not coalesce into a single throughgoing fault may be due to structures in the crust inherited from the assemblage of the Qiangtang and Lhasa terranes along the suture zone. However, the particular setting of the KJFZ in the collision zone may also play an important role. The KJFZ marks the northern border

of a zone of distributed east west extension in the Lhasa terrane with each of its main faults being linked to a major north trending rift to the south, to locally maintain kinematic compatibility.

[41] Another factor that may influence the evolution of the KJFZ is the gradual northward migration of the zone of right-lateral shear as the curvature of the Himalayan arc increases [*Armijo et al.*, 1986, 1989]. Earlier in the history of the collision, right-lateral shear was occurring along the Indus-Yalu suture zone in southern Tibet [*Burg and Chen*, 1984]. This activity probably ceased when the right-lateral shear initiated farther north along the KJFZ during the late Miocene. It is probably around this time that the left-lateral faults in the Qiangtang terrane initiated, leading to the development of the central Tibet conjugate strike-slip fault zone. Farther to the east, the fault system connects with the Jiali and Red River faults allowing the Qiangtang Block and the South China Block to move to the east southeast around the eastern Himalaya syntaxis. This eastward movement initiated when the left-lateral slip ceased on the Red River Fault along with the extrusion of the Indochina Block in the mid-Miocene [*Leloup et al.*, 1995; *Tapponnier et al.*, 1990]. This kinematic relationship is consistent with the model of [*Ratschbacher et al.*, 1996] and recent GPS results from eastern Tibet [*Chen et al.*, 2000; *Shen et al.*, 2005].

6. Conclusions

[42] The surface velocity maps that cover the Dong Co and Bue Co conjugate strike-slip fault systems allow us to characterize the current deformation regime in central Tibet. The slip rates estimated from the InSAR data and the fault geometry indicate that plane strain, right-lateral simple shear is superimposed onto pure shear deformation in a ~200-to 300-km-wide zone running from west to east across central Tibet. This deformation belt includes the KJFZ, previously recognized by *Armijo et al.* [1989], and a series of NE striking left-lateral faults that form conjugate strike-slip fault systems. The deformation regime within the belt is presently accommodating both N10–20°E shortening (pure shear) at a rate of ~5 mm yr^{-1}, and right-lateral simple shear parallel to a N100–120°E direction at a rate of ~6 mm yr^{-1}. Such rates are consistent with previous GPS measurements.

[43] The relatively high slip rates and low magnitude of finite displacement along faults within the Tibetan Plateau, compared to the rates and magnitude of slip along the larger faults that border the northern and western margins of Tibet, suggest that the conjugate strike-slip faults have not been active since the beginning of the Indo-Asian collision. Additionally, the apparent discrepancy between geologic and geodetic fault slip rates in central Tibet may suggest that faults are not in a steady state and that fault slip rates may have accelerated with time. It is suggested that the en echelon fault geometry of the KJFZ may be maintained by the interaction with the rift systems to the south and the progressive migration of right-lateral shear to the north, as the curvature of the Himalayan arc increases and the eastern Himalayan syntaxis migrates northward [*Armijo et al.*, 1986, 1989].

[44] A characteristic feature of the current strain field in central Tibet revealed by the InSAR data is the concentration of the strain in 30- to 60-km-wide zones across the mapped active faults, a feature of the strain field not previously visible in GPS data acquired at sparsely distributed stations [*Wang et al.*, 2001; *Zhang et al.*, 2004]. This observation tends to validate mechanical descriptions of the Tibetan crust as a medium that localizes deformation along faults, defining crustal domains of various sizes that remain relatively undeformed, at least for some period of time.

[45] **Acknowledgments.** We thank Jean-Philippe Avouac, Peter Bird, Paul Kapp, Cecil Lasserre, Gweltaz Maheo, Alex Webb, Alex Robinson, and An Yin for useful comments on an early version of this paper and Eric Fielding and an anonymous reviewer for their detailed and constructive reviews of the manuscript. M.T. expresses thanks to An Yin, Kerry Sieh and the Tectonics Observatory at Caltech for support during various stages of manuscript preparation. This work was supported by the National Science Foundation (EAR 0125688) and the NASA Solid Earth and Natural Hazards Program. Part of G.P.'s work was carried out at the Jet Propulsion Laboratory, California Institute of Technology, under contract with NASA. ERS data were provided by the European Space Agency under a category 1 proposal (CP1316).

References

Armijo, R., P. Tapponnier, J. L. Mercier, and T.-L. Han (1986), Quaternary extension in southern Tibet: Field observations and tectonic implications, *J. Geophys. Res.*, *91*, 13,803–13,872.

Armijo, R., P. Tapponnier, and T.-L. Han (1989), Late Cenozoic right-lateral strike-slip faulting in southern Tibet, *J. Geophys. Res.*, *94*, 2787–2838.

Banerjee, P., and R. Bürgmann (2002), Convergence across the northwest Himalaya from GPS measurements, *Geophys. Res. Lett.*, *29*(13), 1652, doi:10.1029/2002GL015184.

Bendick, R., R. Bilham, J. Freymueller, K. Larson, and G. Yin (2000), Geodetic evidence for a low slip rate in the Altyn Tagh fault system, *Nature*, *404*, 69–72.

Blisniuk, P. M., and W. D. Sharp (2003), Rates of late Quaternary normal faulting in central Tibet from U-series dating of pedogenic carbonate in displaced fluvial gravel deposits, *Earth Planet. Sci. Lett.*, *215*(1–2), 169–186.

Blisniuk, P., B. R. Hacker, J. Glodny, L. Ratschbacher, S. Bi, Z. Wu, M. O. McWilliams, and A. Calvert (2001), Normal faulting in central Tibet since at least 13.5 Myr ago, *Nature*, *412*, 628–632.

Brown, L. D., W. Zhao, K. D. Nelson, M. Hauck, D. Alsdorf, A. Ross, M. Cogan, M. Clark, X. Liu, and J. Che (1996), Bright spots, structure, and magmatism in southern Tibet from INDEPTH seismic reflection profiling, *Science*, *274*, 1688–1690.

Burg, J. P., and G. M. Chen (1984), Tectonics and structural zonation of southern Tibet, China, *Nature*, *311*, 219–223.

Burg, J. P., M. Brunel, D. Gapais, G. M. Chen, and G. H. Liu (1984), Deformation of leucogranites of the crystalline Main Central Sheet in southern Tibet (China), *J. Struct. Geol.*, *6*, 535–542.

Chen, Q., J. T. Freymueller, Q. Wang, Z. Yang, C. Xu, and J. Liu (2004), A deforming block model for the present-day tectonics of Tibet, *J. Geophys. Res.*, *109*, B01403, doi:10.1029/2002JB002151.

Chen, Z., et al. (2000), Global positioning system measurements from eastern Tibet and their implications for India/Eurasia intercontinental deformation, *J. Geophys. Res.*, *105*, 16,215–216,227.

Cheng, J., and G. Xu (1987), Geologic map of the Ritu Region (in Chinese), 598 pp., Tibetan Bur. of Geol. and Miner. Resour., Beijing.

Cowgill, E., A. Yin, T. M. Harrison, and W. Xiao-Feng (2003), Reconstruction of the Altyn Tagh fault based on U-Pb geochronology: Role of back thrusts, mantle sutures, and heterogeneous crustal strength in forming the Tibetan Plateau, *J. Geophys. Res.*, *108*(B7), 2346, doi:10.1029/2002JB002080.

Gehrels, G. E., A. Yin, and X.-F. Wang (2003), Detrital-zircon geochronology of the northeastern Tibetan Plateau, *Geol. Soc. Am. Bull.*, *115*, 881–896, doi:10.1130/0016-7606(2003)115<0881:DGOTNT>2.0.CO;2.

Hanssen, R. (2001), *Radar Interferometry: Data Interpretation and Error Analysis*, 308 pp., Springer, New York.

Harrison, T. M., P. Copeland, W. S. F. Kidd, and O. M. Lovera (1995), Activation of the Nyainqentanghla Shear Zone: Implication uplift of the southern Tibetan Plateau, *Tectonics*, *14*, 658–676.

Jade, S., B. C. Bhatt, Z. Yang, R. Bendick, V. K. Gaur, P. Molnar, M. B. Anand, and D. Kumar (2004), GPS measurements from the Ladakh Himalaya, India: Preliminary tests of plate-like or continuous deformation in Tibet, *Geol. Soc. Am. Bull.*, *116*, 1385–1391, doi:10.1130/B25357.1.

Kapp, P., A. Yin, C. E. Manning, T. M. Harrison, M. H. Taylor, and L. Ding (2003), Tectonic evolution of the early Mesozoic blueschist-bearing Qiangtang metamorphic belt, central Tibet, *Tectonics*, *22*(4), 1043, doi:10.1029/2002TC001383.

Langin, W., et al. (2003), Seismicity of central Tibet from Project INDEPTH III seismic recordings, *Bull. Seismol. Soc. Am.*, *93*, 2146–2159, doi:10.1785/0120030004.

Lasserre, C., G. Peltzer, and F. Crampe (2001), Interseismic strain across the Altyn Tagh Fault System (northern Tibet), Measured by SAR interferometry, *Eos Trans. AGU*, *82*(47), Fall Meet. Suppl., Abstract G31B-0150.

Lee, H., et al. (2003), Miocene Jiali faulting and its implications for Tibetan tectonic evolution, *Earth Planet. Sci. Lett.*, *205*, 185–194.

Leloup, P. H., R. Lacassin, P. Tapponnier, U. Scharer, D. Zhong, X. Liu, L. Zhang, S. Ji, and P. T. Trinh (1995), The Ailao Shan-Red River shear zone (YunnanChina), Tertiary transform boundary of Indochina, *Tectonophysics*, *251*, 3–84.

Masek, J. G., B. L. Isacks, E. J. Fielding, and J. Browaeys (1994), Rift flank uplift in Tibet: Evidence for a viscous lower crust, *Tectonics*, *13*, 659–667.

Métivier, F., Y. Gaudemer, P. Tapponnier, and B. Meyer (1998), Northeastward growth of the Tibet Plateau deduced from balanced reconstruction of two depositional areas: The Qaidam and Hexi Corridor basins, China, *Tectonics*, *17*, 823–842.

Molnar, P., and W. Chen (1983), Focal depths and fault plane solutions of earthquakes under the Tibetan Plateau, *J. Geophys. Res.*, *88*, 1180–1196.

Molnar, P., and H. Lyon-Caen (1989), Fault plane solutions of earthquakes and active tectonics of the Tibetan Plateau and its margins, *Geophys. J. Int.*, *99*, 123–153.

Molnar, P., and P. Tapponnier (1978), Active tectonics of Tibet, *J. Geophys. Res.*, *83*, 5361–5375.

Murphy, M., An. Yin1, P. Kapp, T. M. Harrison, D. Lin, and G. Jinghui (2000), Southward propagation of the Karakoram fault system, southwest Tibet: Timing and magnitude of slip, *Geology*, *28*, 451–454.

Murphy, M. A., A. Yin, T. M. Harrison, S. B. Duerr, Z. Chen, F. J. Ryerson, W. S. F. Kidd, X. Wang, and X. Zhou (1997), Did the Indo-Asian collision alone create the Tibetan Plateau?, *Geology*, *25*, 719–722.

Owens, T. J., and G. Zandt (1997), Implications of crustal property variations for models of Tibetan Plateau evolution, *Nature*, *387*, 37–43.

Peltzer, G., and P. Tapponnier (1988), Formation and evolution of strike-slip faults, rifts, and basins during the India-Asia collision: An experimental approach, *J. Geophys. Res.*, *93*, 15,085–15,117.

Ratschbacher, L., W. Frisch, C. Chen, and G. Pan (1996), Cenozoic deformation, rotation, and stress patterns in eastern Tibet and western Sichuan, China, in *The Tectonic Evolution of Asia*, edited by A. Yin and T. M. Harrison, pp. 227–249, Cambridge Univ. Press, New York.

Rosen, P., S. Hensley, I. Joughin, F. Li, S. Madsen, E. Rodriguez, and R. Goldstein (2000), Synthetic aperture radar interferometry, *Proc. IEEE*, *88*, 333–382.

Rosen, P. A., S. Henley, G. Peltzer, and M. Simons (2004), Updated repeat orbit interferometry package released, *Eos Trans. AGU*, *85*(5), 47.

Savage, J., and R. Burford (1973), Geodetic Determination of Relative Plate Motion in Central California, *J. Geophys. Res.*, *78*, 832–845.

Shen, Z., M. Wang, Y. Li, D. D. Jackson, A. Yin, D. Dong, and P. Fang (2001), Crustal deformation along the Altyn Tagh fault system, western China, from GPS, *J. Geophys. Res.*, *106*, 30,607–30,622.

Shen, Z.-K., J. Lü, M. Wang, and R. Bürgmann (2005), Contemporary crustal deformation around the southeast borderland of the Tibetan Plateau, *J. Geophys. Res.*, *110*, B11409, doi:10.1029/2004JB003421.

Socquet, A., G. Peltzer, and C. Lasserre (2005), Interseismic deformation along the central segment of the Altyn Tagh Fault (Tibet, China) determined by SAR interferometry, *Eos Trans. AGU*, *86*(52), Fall Meet. Suppl., Abstract G53A-0872.

Tapponnier, P., and P. Molnar (1977), Active faulting and tectonics in China, *J. Geophys. Res.*, *82*, 2905–2930.

Tapponnier, P., et al. (1990), The Ailao Shan/Red River metamorphic belt: Tertiary left-lateral shear between Indochina and South China, *Nature*, *343*, 431–437.

Tapponnier, P., Z. Xu, F. Roger, B. Meyer, N. Arnaud, G. Wittlinger, and J. Yang (2001), Oblique stepwise rise and growth of the Tibet Plateau, *Science*, *294*, 1671–1677.

Taylor, M., A. Yin, F. J. Ryerson, P. Kapp, and L. Ding (2003), Conjugate strike-slip faulting along the Bangong-Nujiang suture zone accommodates coeval east-west extension and north-south shortening in the interior of the Tibetan Plateau, *Tectonics*, *22*(4), 1044, doi:10.1029/2002TC001361.

Wallace, K., G. Yin, and R. Bilham (2004), Inescapable slow slip on the Altyn Tagh fault, *Geophys. Res. Lett.*, *31*, L09613, doi:10.1029/2004GL019724.

Wang, Q., et al. (2001), Present day crustal deformation in China constrained by global positioning system measurements, *Nature*, *294*, 574–577.

Wei, W., et al. (2001), Detection of widespread fluids in the Tibetan crust by magnetotelluric studies, *Science*, *292*, 716–718.

Wright, T., et al. (2004), InSAR observations of low slip rates on the major faults of western Tibet, *Science*, *305*, 236–239.

Yin, A., and T. M. Harrison (2000), Geologic evolution of the Himalayan-Tibetan orogen, *Annu. Rev. Earth Planet. Sci.*, *28*, 211–280.

Yin, A., P. A. Kapp, M. A. Murphy, C. E. Manning, T. M. Harrison, M. Grove, D. Lin, X. Deng, and C. Wu (1999), Significant late Neogene east-west extension in northern Tibet, *Geology*, *27*, 787–790.

Zebker, H. A., and R. M. Goldstein (1986), Topographic mapping from interferometric synthetic aperture radar observations, *J. Geophys. Res.*, *91*, 4993–4999.

Zebker, H. A., and J. Vilasenor (1992), Decorrelation in interferometric radar echoes, *IEEE Trans. Geosci. Remote Sens.*, *30*, 950–959.

Zebker, H. A., P. A. Rosen, and S. Hensley (1997), Atmospheric effects in interferometric synthetic aperture radar surface deformation and topographic maps, *J. Geophys. Res.*, *102*, 7547–7564.

Zhang, P., et al. (2004), Continuous deformation of the Tibetan Plateau from global positioning system data, *Geology*, *32*, 809–812, doi:10.1130/G20554.1.

G. Peltzer, Jet Propulsion Laboratory, California Institute of Technology, MS 300-233, 4800 Oak Grove Drive, Pasadena, CA 91109, USA.

M. Taylor, Department of Geology, University of Kansas, 1475 Jayhawk Blvd., 120 Lindley Hall, Lawrence, KS 66045-7613, USA. (mht@ku.edu)